International Journal of Nanomedicine

Dovepress
open access to scientific and medical research

Open Access Full Text Article

ORIGINAL RESEARCH

Efficacy and Molecular Effects of a Reduced Graphene Oxide/Fe_3O_4 Nanocomposite in Photothermal Therapy Against Cancer

This article was published in the following Dove Press journal:
International Journal of Nanomedicine

Claudia C Barrera[1]
Helena Groot[1]
Watson L Vargas[2]
Diana M Narváez[1]

[1]Human Genetics Laboratory, Department of Biological Sciences, Universidad de Los Andes, Bogotá, Colombia; [2]Department of Chemical Engineering, Universidad de Los Andes, Bogotá, Colombia

Purpose: Expanded research on the biomedical applications of graphene has shown promising results, although interactions between cells and graphene are still unclear. The current study aims to dissect the cellular and molecular effects of graphene nanocomposite in photothermal therapy against cancer, and to evaluate its efficacy.

Methods: In this study, a reduced graphene oxide and iron oxide (rGO-Fe_3O_4) nanocomposite was obtained by chemical synthesis. The nanocomposite was fully characterized by Raman spectroscopy, TEM, VSM and thermal profiling. Cell-nanocomposite interaction was evaluated by confocal microscopy and viability assays on cancer cell line HeLa. The efficacy of the thermal therapy and changes in gene expression of Bcl-2 and Hsp70 was assessed.

Results: The resulting rGO-Fe_3O_4 nanocomposite exhibited superparamagnetic properties and the capacity to increase the surrounding temperature by 18–20°C with respect to the initial temperature. The studies of cell-nanocomposite interaction showed that rGO-Fe_3O_4 attaches to cell membrane but there is a range of concentration at which the nanomaterial preserves cell viability. Photothermal therapy reduced cell viability to 32.6% and 23.7% with 50 and 100 µg/mL of nanomaterial, respectively. The effect of treatment on the molecular mechanism of cell death demonstrated an overexpression of anti-apoptotic proteins Hsp70 and Bcl-2 as an initial response to the therapy and depending on the aggressiveness of the treatment.

Conclusion: The results of this study contribute to understanding the interactions between cell and graphene and support its application in photothermal therapy against cancer due to its promising results.

Keywords: reduced graphene oxide, iron oxide, photothermal therapy, cell viability, anti-apoptotic genes, molecular effect

Introduction

Cancer has become one of the principal causes of death around the world. According to WHO in its last report, in 2018, 18.1 million new cases of cancer were estimated, along with 9.6 million related deaths. Furthermore, the International Agency for Research in Cancer (IARC) estimates that, worldwide, the number of new cases will rise to 43.8 million within the next five years.[1] Given this situation, much work has gone into developing new, minimally invasive and more efficient therapies that may reduce side effects in cancer patients. Some of these alternative treatments involve immunotherapy,[2] epigenetic therapy,[3] miRNAs and drug targets,[4,5] and more recently, photothermal therapy. The latter relies on the

Correspondence: Claudia C Barrera
Human Genetics Laboratory, Department of Biological Sciences, Universidad de Los Andes, Cra. 1 # 18a-10, Bogotá, Colombia
Tel +57 1 310 2936500
Email cc.barrera1103@uniandes.edu.co

ability of some materials to absorb light and convert it into enough heat to destroy cancer cells[6,7] due to a phenomenon known as the surface plasmon resonance (SPR) effect.[8] SPR involves the induction of strong surface fields over plasmonic materials due to excitation of electrons caused by electromagnetic radiation. The relaxation of these excited electrons produces heating capable of destroying surrounding cancer cells.[7]

Nanocomposites are the main plasmonic materials used in photothermal therapy. Among them, gold and iron oxide nanoparticles, and carbon nanotubes, have shown optical absorption in the near-infrared (NIR) spectrum.[9] This property provides an advantage since tissues absorb a limited amount of light in the NIR regions; furthermore, NIR is able to penetrate biological tissues more deeply.[6,9] Likewise, the heating of the target region depends on the nanoparticle concentration and on laser power.[10]

Although many research efforts have focused on designing those nanomaterials, the study of the nanocomposite-cell interactions and, more precisely, the molecular mechanism involved with cellular death during the photothermal therapy are still unknown. On one hand, it is thought that temperature rising due to photothermal therapy can induce greater Heat Shock Protein Hsp70[9] activity, which can assist the folding of denatured proteins under conditions of environmental stress.[11] On the other hand, the activation of the intrinsic apoptosis pathway by BCL-2 family proteins that triggers cell phagocytosis[6] has been suggested as part of cellular response to therapy. The BCL-2 family includes both pro-apoptotic and anti-apoptotic groups of proteins involved in keeping the equilibrium between apoptosis and homeostasis. Thus, the activation of the Bcl-2 protein, a member of the anti-apoptotic group, is a good indicator of the treatment effect over cell viability.[12]

Despite the numerous nanomaterials that have been studied and applied in photothermal therapy, graphene is one of the most extensively employed. Graphene is a two-dimensional (2D) sheet of sp^2-bonded carbon[13] that can be synthesized by micromechanical cleavage,[14] Chemical Vapor Deposition (CVD),[15] liquid exfoliation,[16,17] or by Hummers method to obtain graphene oxide (GO), which can be reduced and functionalized.[18] The unique structure of this nanomaterial can lead to some physicochemical properties such as high electronic[15,19] and thermal conductivity, plasmonic properties, large specific surface area, biocompatibility,[20,21] and a great potential for multiple functionalization.[8,22-26] Hence, in this study, we developed and characterized a graphene-based nanocomposite for dual photothermal therapy and bioimaging. The nanostructure was composed by sheets of reduced graphene oxide (rGO) as the photothermal agent, and iron oxide (Fe_3O_4) nanoparticles formed in situ to provide magnetic properties used for magnetic resonance imaging. Thus, the aim of this study was to evaluate nanocomposite-cell interaction by establishing the cytotoxic effect on cervical cancer cell line HeLa, estimating photothermal therapy efficacy, and determining the changes in the expression of Hsp70 and Bcl-2 proteins as an approach to understanding the molecular effects of the therapy.

Materials and Methods

Reagents and Apparatus

Graphite, sodium chloride, potassium ferrocyanide, potassium ferricyanide, sulfuric acid 98%, and other chemical reagents were purchased from commercial companies (Merck or Sigma Aldrich) and used as received. Thiazolyl blue tetrazolium bromide (MTT), DMEM with L-glutamine, phosphate buffer saline (PBS), fetal bovine serum (FBS), and cDNA Reverse Transcription kits were purchased from Thermo Fisher Scientific. Cell and dye cell assay (Kat. Ab115347) was supplied by Abcam. Specific primers for Hsp70 and Bcl-2 proteins were synthetized from specific sequences published elsewhere as follows: Hsp70: 5′-AG GCCAACAAGATCACCATC-3′ (forward) and 5′-TCG TCCTCCGCTTTGTACTT-3′ (reverse);[11] Bcl-2: 5′-TTGT GGCCTTCTTTGAGTTCGGTG-3′ (forward) and 5′-GGT GCCGGTTCAGGTACTCAGTCA-3′ (reverse);[27] β-actin: 5′-CGGAACGGCTCATTGCC-3′ (forward) and 5′-AC CCACACTGTGCCCATCTA-3′ (reverse). The HeLa cells were obtained from the ATCC.

TEM micrographs were performed using JEOL-1400Plus Transmission electron microscopy. Elemental analysis EDS (Energy Dispersive Spectrometer) was carried out using the Phenom ProX desktop scanning electron microscope (SEM). Magnetic properties were measured with a Vibrating Sample Magnetometer (VSM) LakeShore model 7404. Raman spectroscopy was carried out using a HORIBA Raman microscope instrument model XploRA. Photothermal capacity of nanomaterial was recorded using a Thermal imaging camera Micro-Epsilon model TIM 160. Confocal micrographs of nanomaterial–cell interaction were performed using an Olympus FluoView FV1000 confocal microscope.

Synthesis of GO

GO was prepared using a modified Hummer's method according to literature.[28] One gram of graphite (1 g) powder was ground with 50 g NaCl for 10 min. The mixture was washed with water and graphite was recovered by filtration. The remaining solid was stirred in 23 mL of H_2SO_4 (98%) for 8 h. Then, 3 g $KMnO_4$ was gradually added in an ice bath. The mixture was then stirred at 35–40°C for 30 min, and then at 65–80°C for 45 min. Next, 46 mL of water was added and the mixture heated at 98–105°C for 30 min. The reaction was stopped by adding 140 mL of distilled water and 10 mL of H_2O_2 (30%). The mixture was washed by repeated centrifugation and filtration, first with 5% HCl aqueous solution, and then distilled water. The final product was dried under vacuum.

Preparation of rGO-Fe_3O_4 Composite

The rGO-Fe_3O_4 composite was synthesized as reported previously.[29] Briefly, 0.7 g GO was dissolved in 450 mL of water. Concurrently, 0.4055 g $FeCl_3$ and 0.1584 g $FeCl_2$ were dissolved in 25 mL of water and the solution was slowly added to the aqueous GO. Then, 30% ammonia was added to this mixture to adjust pH to 10. The temperature of this solution was raised to 90°C and 10 mL of hydrated hydrazine was added under constant stirring resulting in an rGO. The mixture was stirred for 4 h and cooled to room temperature. The rGO-Fe_3O_4 product was washed and filtered with water and ethanol several times and the final product was dry under vacuum.

Material Characterization

The morphology of rGO-Fe_3O_4 was examined by TEM dispersing the composite in water and a sample dropped on a copper grid; meanwhile, the composition of the nanomaterial was studied by means of an EDS analysis. Magnetic properties and configurations were defined using a VSM among -1.5×10^4 to 1.5×10^4 G and Raman Spectroscopy, respectively. In order to study the thermal activity, two concentrations of the nanocomposite (50 and 100 µg/mL) were irradiated with an 804 nm optical laser at a power density of 1 W/cm^2 for 5 min. The temperature was recorded with a thermal imaging camera.

Cytotoxicity Assays

Cytotoxicity was measured in vitro using standard MTT, trypan blue staining and Calcein AM assays. HeLa cells were seeded into 96-well cell-culture plates at 2×10^5 cells/mL and then cultured in Dulbecco's Modified Eagle Medium (DMEM) and supplemented with 10% of heat-inactivated FBS and 1% of antibiotics. Cells were incubated at 37ºC with 5% of CO_2 in a humidified atmosphere for 24 h. After incubation, concentrations between 10 µg/mL and 1 mg/mL of nanomaterial-culture media solution were added and incubated for a further 48 h. Cultured cells without rGO-Fe_3O_4 in the media were used as negative control. Then, the standard MTT, Calcein AM assay and trypan blue exclusion tests were conducted to determine the cell viability. The results were expressed as the percentage of living cells calculated assuming the results of control cells as 100%. LD50 was estimated by fitting a polynomial regression model to the results and evaluating the concentration of the nanocomposite at which 50% of the cells remain alive.

Photothermal Therapy in vitro

For photothermal therapy, HeLa cells were incubated, as mentioned earlier, for 24 h. These cells were seeded in a culture plate at 2-well intervals to avoid heating interference from the other experiments. Then, 50 µg/mL and 100 µg/mL of rGO-Fe_3O_4 were added to the cultured cells and these were incubated for 2 h. Next, the seeded wells were irradiated with an 804 nm laser, at a power density of 1 W/cm^2 for 5 min. Finally, a standard MTT assay was conducted to determine the cell-killing efficacy after therapy.

mRNA Quantification (qPCR)

HeLa cells were incubated in petri dishes (3.5 cm of diameter) and exposed to 50 µg/mL and 100 µg/mL of rGO-Fe_3O_4 as described above. After treatment, total RNA was extracted and purified using Trizol. The cDNA synthesis was performed using a cDNA Reverse Transcription Kit according to the manufacturer's instructions. The qPCR was conducted using Power SYBR Green PCR Master Mix, and specific selected primers for Hsp70 and Bcl-2 were used. β-actin was the housekeeping gen. The thermal protocol consisted of 10 min polymerase activation at 95°C, 40 cycles of denaturation (15 s at 95°C) and 1 min combined stringed annealing/extension at 60°C. Data were evaluated with the $2^{-\Delta\Delta C_T}$ method[30] and analyzed statistically.

Statistical Analysis

Data were analyzed in GraphPad Prism 8.4.1 using one or two-way ANOVA with Dunnet's or Sidak's multiple comparison to establish the difference between the treatments and control. For all tests the significance level α was 0.05.

Results and Discussion

Characterization of rGO-Fe_3O_4 Nanocomposite

The rGO-Fe_3O_4 was synthesized by precipitation of iron oxide nanoparticles onto water-soluble GO sheets and coupled reduction to rGO. Raman spectroscopy data (Figure 1A) confirmed the structure of rGO reported in the literature for graphene composites reduced by different methods and decorated with magnetic nanoparticles.[29,31-34] As expected, an intense D band was found at 1340 cm^{-1} and a characteristic G band was found at 1585 $cm^{-}1$. The D band is associated with structural defects, amorphous carbon, functional groups or edges that can break the symmetry, while the G band is related to the vibrational mode of sp^2 hybridized carbon atoms.[29,33,35] As studied previously, in contrast with GO, rGO exhibits a higher D band which can be expressed in terms of the ratio I_D/I_G used as a measure of the level of defects and disorder.[33] In this case, the I_D/I_G ratio for the rGO-Fe_3O_4 is 1.3, as expected, which indicates the presence of localized sp^3 defects within the sp^2 carbon network upon reduction of the exfoliated GO and the Fe_3O_4 nanoparticles embedded in the rGO sheets.[29,33] Furthermore, a 2D peak was found around 2680 cm^{-1} as a second-order Raman process that results from a two phonon lattice vibrational process.[36] These results provide the presence of defects relative to strong redox processes. Moreover, width, position and ratio of 2D and G bands indicate the configuration of a graphene with few disorder layers.[37]

The morphology of nanocomposite was also characterized by TEM. Micrographs showed iron oxide nanoparticles with a diameter of 4–20 nm deposited on the rGO surface, and sheets with a size of around 0.8 and 2.5 µm with 2–5 layers (Figure 1B and C) as predicted by Raman Spectroscopy. Additionally, the results of the EDS analysis demonstrated that rGO-Fe_3O_4 was composed by almost 4.825% Fe, 25.05% O and 70.125% C, as expected.

Magnetic properties of rGO-Fe_3O_4 were initially proved with the exposure of nanocomposite in aqueous solution to an external magnetic field (Figure 1D). As shown, the material becomes magnetized immediately at the external field exposure, but once it is removed, the nanocomposite no

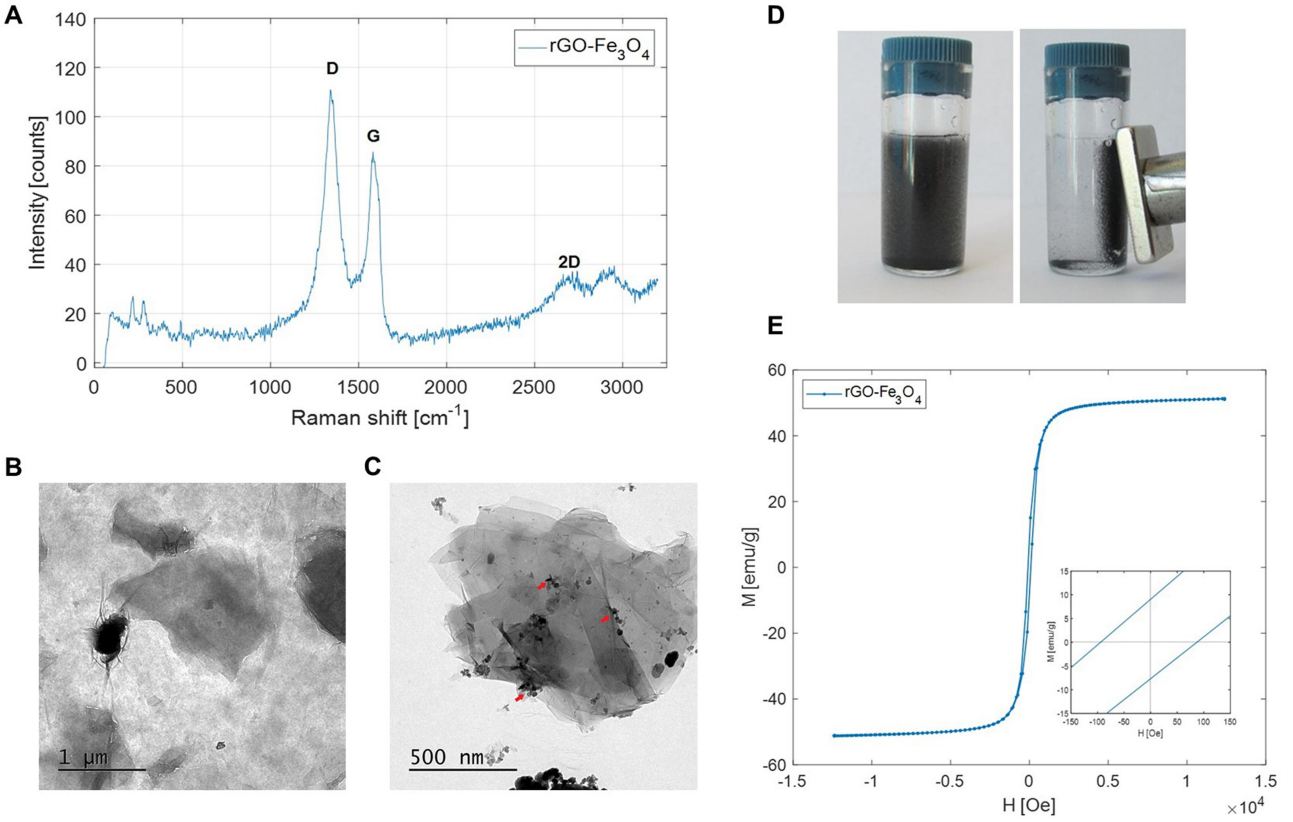

Figure 1 Results of the characterization test for the nanocomposite (**A**) Raman spectroscopy of rGO-Fe_3O_4, (**B**) TEM micrographs before and (**C**) after reduction of graphene oxide and simultaneous attaching of Fe_3O_4 nanoparticles. Red arrows point Fe_3O_4. (**D**) Visual response of the nanocomposite dissolved in water and exposed to an external permanent magnetic field. (**E**) Magnetic characterization by VSM at room temperature. The inset shows close view of hysteresis loop.

longer exhibits any residual magnetism. This result was confirmed with the VSM test, which suggests a minimal hysteresis loop with a low remnant magnetization (M_R) and coercivity (H_C) (Figure 1E) similar to other graphene-iron nanocomposites produced using different methods (Table 1). By comparison, those nanocomposites with more metals embedded in the graphene matrix exhibit higher coercivity. However, the rGO-Fe_3O_4 produced in this work shows a high saturation magnetization (M_S) similar to those nanocomposites with cobalt.[32,38,39] According to this observation, the nanocomposite could be considered a superparamagnetic material as it can result in a magnetic response on application of an external magnetic field and negligible remanence and coercivity in absence of the field.[40] Such characteristics make this material a promising target as magnetic resonance contrast agent for MR imaging.

Cytotoxicity Assessment of rGO-Fe_3O_4

Numerous studies have demonstrated that nanomaterials may potentially affect the results of cytotoxicity assays due to their high adsorption and optical activity.[44–46] To prevent false evaluation of cell viability, both MTT, trypan blue, and Calcein AM assays were used to assess cytotoxicity within a range of concentrations from 10 µg/mL to 1 mg/mL of the nanocomposite. For all assays and after 48 h of exposure, cell viability decreased in a dose-dependent manner (Figure 2). A statistically significant difference was found between controls and concentrations of above 50 µg/mL for all tests, as well as significant differences between the various assays. Thus, the viability results obtained using Trypan blue staining appear to be higher than those obtained using the other methods. This can be due to the fact that while Trypan blue exclusion test only considers the integrity of the cell membrane to differentiate between live and dead cells, the other methods also assess the metabolic activity of the cell. It is therefore possible that cells that maintain an integer cell membrane might have a reduced or even null metabolic activity. These results are in line with previously reported studies, which established that rGO causes less membrane damage because it has a low oxidation state and few reactive surface groups.[47,48]

On the other hand, the differential results between the MTT and Calcein AM assays can be related to the interference of the rGO-Fe_3O_4 nanocomposite with the reactants of the test. In relation to this observation, most authors coincide with the idea that the alterations in MTT assays are associated to three factors: adsorption, electron transfer, and optical interferences caused by the graphene. The large surface area of GO and its capability to adsorb surrounding compounds through π-π and electrostatic interaction might facilitate the attachment of MTT to the rGO-Fe_3O_4.[46] As a result, if the nanocomposite concentration is sufficiently high, it could adsorb a broad percentage of MTT which will be less available for cells altering the viability results to high concentrations. This can explain the elevated results of cell viability tested with MTT after 100 µg/mL compared with Calcein AM. Moreover, given the insufficient reduction of the GO and the interaction with the functional groups in the surroundings, there may be electrons in its matrix. These electrons can react with the cation $[MTT]^+$ to produce an intermediate radical $[MTT]^{\bullet}$ that can react with the surrounding protons, generating a protonated cation$[MTTH]^+$. This intermediate product reacts with other electrons in the nanocomposite and produces [FORMH] which, following an additional protonation, results in$[FORMH]^+$, as explained Liao and collaborators.[45] Consequently, formazan could be produced by the nanocomposite which also increases the viability results. Finally, it was stated that the optical properties of graphene, such as absorption and reflection, can augment due to the configuration of more layers[46,49] as in this case.

Table 1 Parameters of the Hysteresis Loop for rGO-Fe_3O_4 and Similar Nanocomposites from Other Studies

Nanocomposite	Production Method	M_s [emu/g]	M_R [emu/g]	H_C [Oe]	Ref.
rGO-Fe_3O_4	Chemical reaction with magnetite and reduction with hydrazine	51.1	9.8	88.1	(this work)
M-RGO	Chemical reaction with magnetite and reduction with hydrazine	22.3	0.3	12.0	[29]
CFO/rGO	Solvothermal method	53.5	12.9	347.5	[32]
GO–Fe_3O_4	Inverse chemical co-precipitation	69.3	13.2	114.0	[41]
RGO-$CoFe_2O_4$	Simple reaction with $NaBH_4$	53.6	25.3	768.0	[38]
rGO/Fe_3O_4 NC	Solvothermal method	19.7	1.4	60.4	[42]
CoOx@C-rGO	Solvothermal method and calcination with glucose	70.6	14.1	399.9	[39]
RGO/$Sr_2CuMgFe_{28}O_{46}$	Green sol-gel method	18.6	10.9	4803.0	[43]

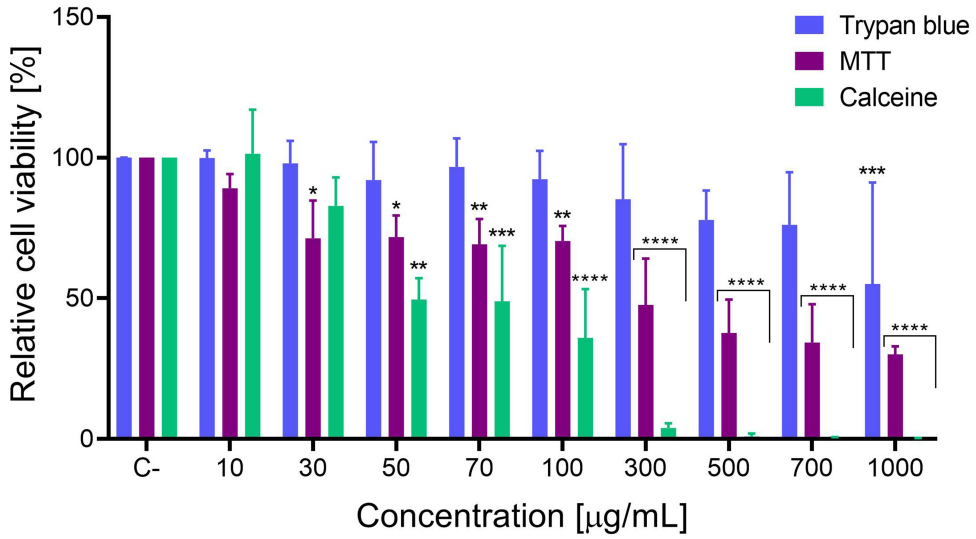

Figure 2 Cytotoxicity evaluation. Relative cell viability evaluated by trypan blue, MTT and Calcein AM assays. Statistical analysis was conducted using two-way ANOVA and a Dunnet's multi comparison test. * is used for p-value < 0.05, ** for p-value < 0.01, *** for p-value < 0.001 and **** for p-value < 0.0001. Error bars depict SD of data.

Although these factors might explain the increased values of the MTT assays when compared to those of the Calcein AM test, a steep decrease is observed for both assays after 100 µg/mL and a relatively stable behavior after 300 µg/mL. This drastic reduction in cell viability could be explained by the use of toxic reagents, such as hydrazine or sulfuric acid, of which traces remain in the nanocomposite, increasing cytotoxicity.[50] As a solution to this issue, many authors have proposed the use of an eco-friendly graphene oxide reduction to avoid the use of toxic reagents.[51,52] The LD50 found was 84.2 µg/mL and 236.2 µg/mL for the Calcein and MTT assays, respectively. No LD50 was analyzed using the trypan blue test.

Nanocomposite-Cell Interaction

Nanocomposite-cell interaction was studied using confocal fluorescent micrographs and Live and Dead Cell Assay such as fluorescent dye, which labels viable cells green. Images reveal two cases, one where rGO-Fe_3O_4 flakes can be seen as dark aggregates grounded to the cell membranes and another where the location of nanocomposite corresponds with intense fluorescent zones (Figure 3 and Supplementary data Figure S1). The latter may be related to the fact that GO has an excellent absorption capability and can exhibit optical properties (such as light absorption and reflection) that increase with the number of layers of the conjugate, as explained above.[49] As seen, most of the graphene flakes attach to the cell membrane suggesting that this material could be an excellent drug carrier; furthermore, a possible penetration of the nanocomposite can be mediated for the irregular boundaries of the graphene and the spontaneous interaction between the hydrophobic matrix and the non-polar inner membrane.[47,53] However, it was not possible to observe cell uptake of the nanocomposite and no membrane damage or change in the morphology was found (Figure 3 and Supplementary data Figure S2). These results were confirmed using the Trypan blue viability test (Figure 2), as mentioned earlier, and are in line with previous studies that attribute the negative interactions between graphene oxide and lipids in the cell membrane to the electrostatic charge between them,[54] when compared to the more hydrophilic surface of rGO.[47]

Photothermal Behavior of rGO-Fe_3O_4

In order to investigate the photothermal activity of rGO-Fe_3O_4, two different concentrations of nanocomposite solution (50 µg/mL and 100 µg/mL) were irradiated with an 804 nm optical laser at a power density of 1 W/cm^2 for 5 min, and compared with water and PBS as controls (Figure 4A and Supplementary Video S1). Temperatures in all treatments were normalized on the same initial temperature (room temperature) to allow comparison. The temperature change of both rGO-Fe_3O_4 concentrations rapidly increased by around 18°C with respect to the initial temperature. Meanwhile, the results for temperature change for water and PBS were almost negligible. The fact that temperature changes were independent of concentration could be associated with the insoluble nature of the conjugate. Thus, the final irradiated zone may not be at the initial concentration

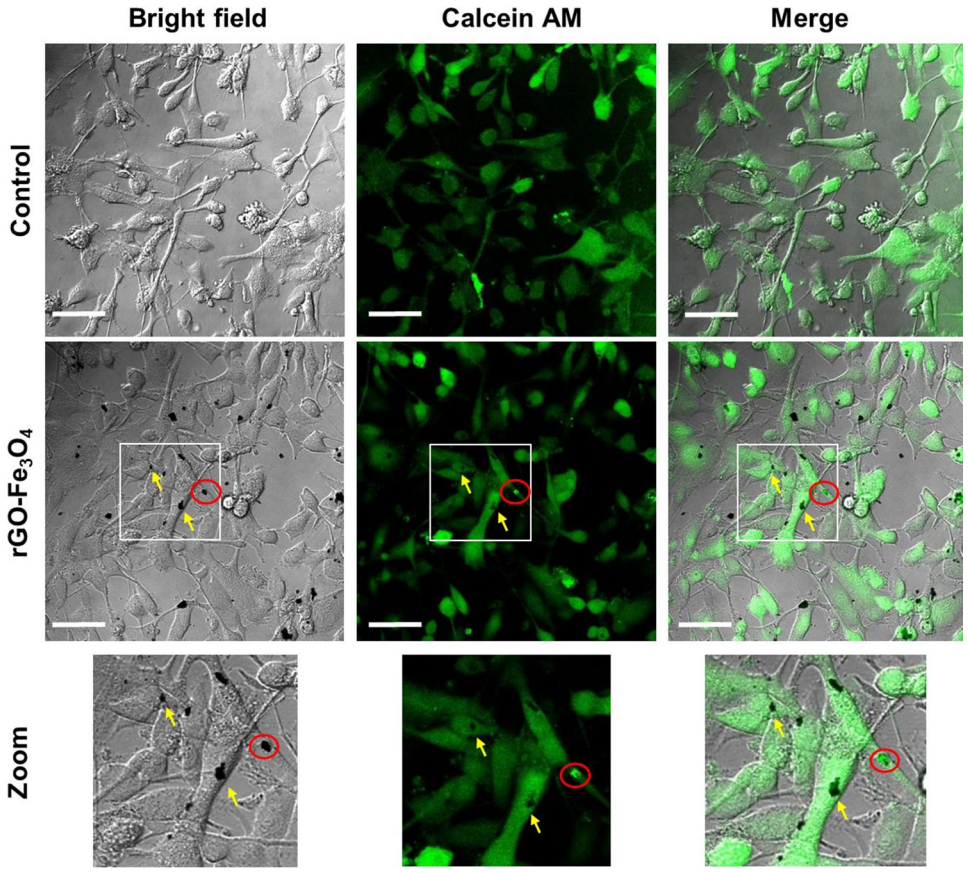

Figure 3 Interaction between cells and graphene nanocomposite. Fluorescent confocal micrographs of HeLa cells with the nanocomposite pointed with yellow arrows for dark aggregates and rounded in red for intense fluorescent deposits. The area enclosed in white squares is zoomed in the last row. Scale bar is 5 µm.

due to solution precipitation. However, a comparison with similar graphene-based materials (Table 2) reveals that the rGO-Fe_3O_4 produced can increase the temperature to values close to the other nanocomposites under similar irradiation conditions and concentrations. More importantly, the synthetized nanocomposites can present a temperature increase of over 18°C in just 5 minutes and with no extra photosensitizing agents. Therefore, taking into account that normal tissue temperature is around 37°C, the rGO-Fe_3O_4 can reach 50°C, which is considered a cell-killing temperature.[55]

Furthermore, images captured with the thermal camera demonstrated two important results. The first is that photothermal capacity is provided by the graphene solution alone and not by the container (Figure 4B and Supplementary Video S2). The second refers to the focalized photothermal response of the material to irradiation which will allow the use of the nanocomposite for cellular ablation with minimal side effects in the neighboring cells.

Photothermal Therapy Efficacy

Having evaluated the in vitro cytotoxicity of the nanocomposite and established a concentration interval of minimum toxicity, the photothermal therapeutic response was examined. HeLa cells were treated with rGO-Fe_3O_4 (50 µg/mL and 100 µg/mL) for 2 h, and then exposed to an 804 nm laser, at a power density of 1 W/cm^2 for 5 min. Viability was determined by an MTT assay. Results show that photothermal therapy with the nanocomposite reduces cell viability to 32.6% and 23.7% with 50 and 100 µg/mL, respectively (Figure 5A). Untreated cells were not noticeably affected, and even under laser exposure, viability was maintained over 83%. Additionally, the rapid temperature increase from 21.9°C to 43.1°C (Figure 4B) reveals the enhanced cancer cell-killing efficacy of rGO-Fe_3O_4. A significant difference was found for 100 µg/mL when compared to the control. Analysis was conducted using a one-way ANOVA and a Dunnet's multiple comparison test.

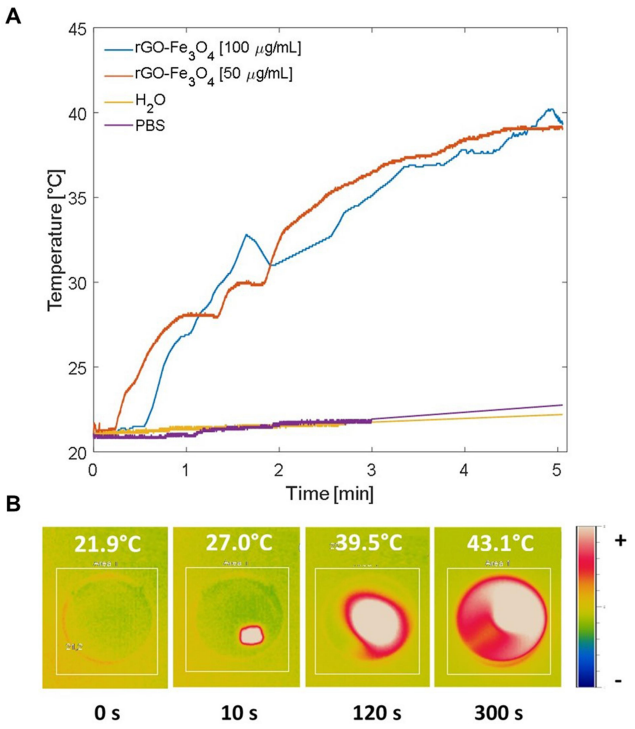

Figure 4 Photothermal behavior of the nanocomposite. (**A**) Temperature profile of the rGO-Fe_3O_4 dissolved in water and increasing the surroundings temperature while it is irradiated with an 804 nm optical laser (1 W/cm^2 for 5 minutes). Temperatures in all treatments were normalized to the same initial room temperature (21.1°C). (**B**) Thermal images of the nanocomposite (100 μg/mL) contained in a petri dish (35 mm) and under the same irradiation conditions. The temperature described is the highest temperature in the dish.

It is noteworthy that even if the rGO-Fe_3O_4 produced does not reach the highest rise of temperature among similar graphene-based materials (Table 2), it is able to reach one of the best results of cellular ablation after photothermal therapy in only 5 minutes and at a low concentration. This, considering that nanocomposites such as GO/$MnWO_4$/PEG[59] or GO-PEG(TP),[62] which show the lowest cell viabilities after photothermal treatment, use concentrations of 200 μg/mL and 1 mg/mL, respectively, as well as irradiation times of 10 minutes.

Photothermal Effect on Anti-Apoptotic Gene Expression

According to mRNA quantification, the results show no patterns related to the concentration of the rGO-Fe_3O_4 and the expression of the studied genes. However, it is possible to observe that for all treatments both genes are overexpressed in comparison with the control, except for Bcl-2 with 50 μg/mL which is underexpressed. Statistical analysis displays significant differences between 100 μg/mL treatment in the Bcl-2 gene and the control and 50 μg/mL treatments (Figure 5B). No significant differences were found for any other treatments or among genes, although remarkable overexpression of the genes was observed under laser irradiation without nanocomposite. This reflects that the effect of NIR light is not as negligible for cells as expected, and it activates anti-apoptotic pathways to avoid cell death.

Previous studies related to the molecular mechanism of apoptosis during photothermal therapy demonstrated that the principal factor involved in this process is the increased level of Reactive Oxygen Species (ROS).[48,65,66] ROS induces apoptosis pathway, avoiding necrosis and consequently an inflammatory response. Although, on in vitro models, the apoptosis signals are ignored because of the absence of phagocytic cells, the initial primary apoptosis becomes secondary necrosis.[6] Hence, it is reasonable to infer that the first responses of cell to the therapy will be guided to control stress induced by rising temperature and apoptosis.

Hsp70 has attributed pleiotropic activities such as molecular chaperon and anti-apoptotic protein,[67] and its pattern of expression reflects this hypothesis. Thus, the Hsp70 gene is overexpressed when the treatment is more aggressive to counteract the therapy effect during or immediately after its application. Thus, some studies have used this gene as an indicator of treatment efficacy because it is upregulated under extreme heat stress.[68] A number of studies have also included inhibitors of the HSP family to prevent initial thermal resistance of the cancer cell and enhance photothermal therapy.[64,69] Other studies, however, reveal that some time after treatment, the expression levels decay as this protein is insufficient in compensating the damage caused by the rising temperature.[9]

On the other hand, the expression of Bcl-2 decreased at 50 μg/mL and increased at 100 μg/mL probably because of the following two factors: the unknown expression of pro-apoptotic protein and the activity of other anti-apoptotic proteins of the BCL-2 family. With respect to the first factor, the study of pro-apoptotic proteins (as Bak or Bax) would make it possible to define the activation of an apoptotic cascade based on the pro-apoptotic/anti-apoptotic protein relationship.[70–72] In fact, most studies agree with the result that photothermal therapy upregulates pro-apoptotic genes and downregulates anti-apoptotic genes.[66,73] On the other hand, the BCL-2 family involves 6 anti-apoptotic proteins: Bcl-2, Bcl-xL, Bcl-B, Bcl-W, Bfl-1and Mcl-1, with Mcl-1 being the most expressed in HeLa cells.[74] Thus, it is possible

Table 2 Irradiation Condition, Maximum Temperature Difference, and Cell Viability After Photothermal Therapy with Different Graphene-Based Nanocomposites

Nanocomposite	Concentration [μg/mL]	Irradiation Conditions (Wavelength, Power or Power Density, Duration)	Maximum ΔT[°C]	Cell line	% Cell Viability After Treatment	Ref.
rGO-Fe_3O_4	50	804 nm, 1 W/cm^2, 5 min	18.0	HeLa	32.6%	(this work)
	100		18.3		23.7%	
mGO-CS/SA	50	808 nm, 1 W/cm^2, 5 min	18.0	A549	26.9%	[56]
	100		23.5		27.4%	
N-O-CDs	200	808 nm, 0.8 W/cm^2, 5 min	32.2	HeLa	13.0%	[57]
GO-IONP-CS /DEX	50	808 nm, 1 W/cm^2, 5 min	17.5	A549	28.1%	[58]
GO/$MnWO_4$/PEG	200	808 nm, 0.6 W/cm^2, 15 min	26.5	4T1	11.0%*	[59]
GQDs-Fe/Bi NPs	50	808 nm, 1.7 W/cm^2, 10 min	15.0	HeLa	68.0%	[55]
	100		28.5		50.0%	
Cu_2−xSe@rGO	50	980 nm, 1.0 W, 10 min	23.5	HEp-2	70.0%	[60]
MGBP	100	808 nm, 1 W/cm^2, 10 min	35.0	HeLa	22.0%	[61]
GO-PEG(TP)	50	980 nm, 0.5 W/cm^2, 10 min	21.5	4T1	16.0%**	[62]
9T-GQDs	100	1064 nm, 1.0 W/cm^2, 5 min	18.0	4T1	43.0%	[63]
GO/$BaHoF_5$/PEG	100	808 nm, 0.4 W/cm^2, 10 min	12.8	HeLa	35.0%	[64]

Notes: *Irradiation duration for cell viability assay was 10 min. **Concentration of nanocomposite for cell viability assay was GO-PEG = 1 mg/mL and TP = 1 mmol/L.

that for the treatment with the lowest concentration of the nanocomposite, the anti-apoptotic activity is controlled by the constitutive Mcl-1 protein, while with more aggressive treatment this protein could require the help of Bcl-2 to counteract the therapy effects.

Conclusion

In this study, an rGO-Fe_3O_4 nanocomposite was successfully produced using the modified Hummers method and functionalized with the deposition of iron oxide nanoparticles. This material exhibits superparamagnetic properties due to the presence of Fe_3O_4 and is able to increase the temperature of the surroundings when irradiated with an 804 nm optical laser. Both characteristics make this material a promising option for use as a contrast agent in MR imaging and thermal ablation of cancer cells. Although cytotoxicity assays compared using three different methods show that viability decreases in a dose-depended manner, the reduction rate obtained in the different tests was not consistent. This could be due to the working principles of each assay and the interferences caused by the graphene nanocomposite, some of them related to its physicochemical characteristics and to the cell–graphene interaction. Further, the test conducted on photothermal activity demonstrated a promising efficacy of the treatment as it was able to reduce cancer cell viability to

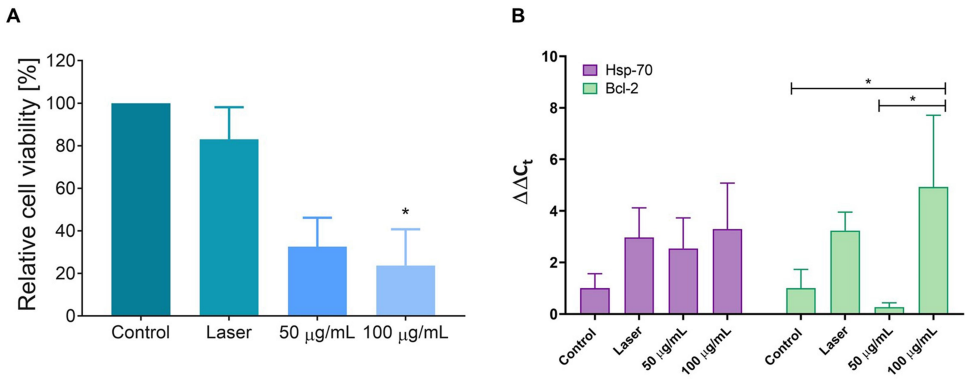

Figure 5 Effect of the photothermal therapy. (**A**) Efficacy of the therapy evaluated as the relative cell viability. Analysis was conducted using one-way ANOVA and a Dunnet's multiple comparison test. (**B**) Relative expression of mRNA of Hsp70 and Bcl-2 genes using β-actin as housekeeping gen. Statistical analysis was conducted using two way ANOVA with Sidak's multiple comparison test. * refers to a p-value < 0.05. Error bars depict SD of data.

32.6% and 23.7% with nanocomposite concentrations of 50 µg/mL and 100 µg/mL, respectively. Additionally, the effect of the therapy on gene expression seems to be involved in initial overexpression of anti-apoptotic proteins as an initial defense mechanism. Nonetheless, further studies on gene expression levels after treatments are necessary involving pro-apoptotic proteins and time monitoring. Finally, it was found that rGO-Fe_3O_4 tends to aggregate on the cell membrane but further research is required, which focuses on nanocomposite-cell interactions.

Acknowledgments

We would like to thank the Department of Chemical Engineering (Universidad de los Andes) for allowing us to use the laser and the thermal camera, the Department of Chemistry (Universidad de los Andes) for conducting the Raman spectroscopy analysis, and to the Hospital Universitario Fundación Santa Fe de Bogotá for performing the TEM microscopy. We especially thank Doctor Fernando Pastrana for his advice and support.

Disclosure

Watson L. Vargas reports the company in which they currently serve as Director of Innovation is related to the health sector, but that the submitted contribution is not related with their current line of business. The authors report no other potential conflicts of interest in this work.

References

1. IARC Global Cancer Observatory. Press release N° 263; 2018. Available from: http://gco.iarc.fr/. Accessed October 21, 2019
2. Lepisto AJ, Mckolanis JR, Finn OJ. Chapter 10 – cancer Immunotherapy: challenges and opportunities. In: *Cancer Immunotherapy*; 2007:167–181. doi:10.1016/B978-012372551-6/50074-2
3. Yoo CB, Jones PA. Epigenetic therapy of cancer: past, present and future. *Nat Rev Drug Discov*. 2006;5(1):37–50. doi:10.1038/nrd1930
4. Pereira DM, Rodrigues PM, Borralho PM, Rodrigues CMP. Delivering the promise of miRNA cancer therapeutics. *Drug Discov Today*. 2013;18(5):282–289. doi:10.1016/j.drudis.2012.10.002
5. Yang X, Zhang X, Ma Y, Huang Y, Wang Y, Chen Y. Superparamagnetic graphene oxide–Fe3O4 nanoparticles hybrid for controlled targeted drug carriers. *J Mater Chem*. 2009;19(18):2710. doi:10.1039/b821416f
6. Pérez-Hernández M, Del Pino P, Mitchell SG, et al. Dissecting the molecular mechanism of apoptosis during photothermal therapy using gold nanoprisms. *ACS Nano*. 2015;9(1):52–61. doi:10.1021/nn505468v
7. Huang X, El-Sayed MA. Plasmonic photo-thermal therapy (PPTT). *Alexandria J Med*. 2011;47(1):1–9. doi:10.1016/j.ajme.2011.01.001
8. Shi X, Gong H, Li Y, Wang C, Cheng L, Liu Z. Graphene-based magnetic plasmonic nanocomposite for dual bioimaging and photothermal therapy. *Biomaterials*. 2013;34(20):4786–4793. doi:10.1016/j.biomaterials.2013.03.023
9. Yang L, Tseng YT, Suo G, et al. Photothermal therapeutic response of cancer cells to aptamer-gold nanoparticle-hybridized graphene oxide under NIR illumination. *ACS Appl Mater Interfaces*. 2015;7(9):5097–5106. doi:10.1021/am508117e
10. Lal S, Clare SE, Halas NJ. Photothermal therapy: impending clinical impact. *Acc Chem Res*. 2008;41(12):1842–1851. doi:10.1021/ar800150g
11. Liu Y, Li N, Li Y, Li H, Wang X. HSP70 is associated with endothelial activation in placental vascular diseases. *Mol Med*. 2008;14(9–-10):1. doi:10.2119/2008-00009.Liu
12. Alberts B, Johnson A, Lewis J, Raff M, Roberts K, Walter P. *Molecular Biology of the Cell*. Vol. 1. Fifth ed. Anderson M, Granum S eds.Garland Science, Taylor & Francis Group; 2008. doi:10.1017/CBO9781107415324.004
13. Geim AK, Novoselov KS, The rise of graphene. *Nat Mater*. 2007;6(3):183–191. doi:10.1038/nmat1849
14. Lotya M, Hernandez Y, King PJ, et al. Liquid phase production of graphene by exfoliation of graphite in surfactant/water solutions liquid phase production of graphene by exfoliation of graphite in surfactant/water solutions. *J Am Chem Soc*. 2009;131(11):3611–3620. doi:10.1021/ja807449u
15. Zhang Y, Zhang L, Zhou C. Review of chemical vapor deposition of graphene and related applications. *Acc Chem Res*. 2013;46(10):2329–2339. doi:10.1021/ar300203n
16. Coleman JN. Liquid exfoliation of defect-free graphene. *Acc Chem Res*. 2012;6(1):14–22. doi:10.1021/ar300009f
17. Paton KR, Varrla E, Backes C, et al. Scalable production of large quantities of defect-free few-layer graphene by shear exfoliation in liquids. *Nat Mater*. 2014;13(6):624–630. doi:10.1038/nmat3944
18. Hummers WS, Offeman RE. Preparation of graphitic oxide. *J Am Chem Soc*. 1958;80(6):1339. doi:10.1021/ja01539a017
19. Sun Z, James DK, Tour JM. Graphene chemistry: synthesis and manipulation. *J Phys Chem Lett*. 2011;2(19):2425–2432. doi:10.1021/jz201000a
20. Jahanbani S, Benvidi A. A novel electrochemical DNA biosensor based on a modified magnetic bar carbon paste electrode with Fe3O4NPs-reduced graphene oxide/PANHS nanocomposite. *Mater Sci Eng C*. 2016;68:1–8. doi:10.1016/j.msec.2016.05.056
21. Gollavelli G, Chang CC, Ling YC. Facile synthesis of smart magnetic graphene for safe drinking water: heavy metal removal and disinfection control. *ACS Sustain Chem Eng*. 2013;1(5):462–472. doi:10.1021/sc300112z
22. Ma X, Tao H, Yang K, et al. A functionalized graphene oxide-iron oxide nanocomposite for magnetically targeted drug delivery, photothermal therapy, and magnetic resonance imaging. *Nano Res*. 2012;5(3):199–212. doi:10.1007/s12274-012-0200-y
23. Tian T, Shi X, Cheng L, et al. Graphene-based nanocomposite as an effective, multifunctional, and recyclable antibacterial agent. *ACS Appl Mater Interfaces*. 2014;6(11):8542–8548. doi:10.1021/am5022914
24. Amjadi M, Manzoori JL, Hallaj T. Chemiluminescence of graphene quantum dots and its application to the determination of uric acid. *J Lumin*. 2014;153:73–78. doi:10.1016/j.jlumin.2014.03.020
25. Chen ML, He YJ, Chen XW, Wang JH. Quantum-dot-conjugated graphene as a probe for simultaneous cancer-targeted fluorescent imaging, tracking, and monitoring drug delivery. *Bioconjug Chem*. 2013;24(3):387–397. doi:10.1021/bc3004809
26. Patil AJ, Vickery JL, Scott TB, Mann S. Aqueous stabilization and self-assembly of graphene sheets into layered bio-nanocomposites using DNA. *Adv Mater*. 2009;21(31):3159–3164. doi:10.1002/adma.200803633
27. Paul-Samojedny M, Kokocińska D, Samojedny A, et al. Expression of cell survival/death genes: bcl-2 and bax at the rate of colon cancer prognosis. *Biochim Biophys Acta Mol Basis Dis*. 2005;1741(1):25–29. doi:10.1016/j.bbadis.2004.11.021
28. Sun X, Liu Z, Welsher K, et al. Nano-graphene oxide for cellular imaging and drug delivery. *Nano Res*. 2008;1(3):203–212. doi:10.1007/s12274-008-8021-8

29. Chandra V, Park J, Chun Y, Lee JW, Hwang I, Kim KS. Water-dispersible magnetite-reduced graphene oxide composites for arsenic removal. *ACS Nano*. 2010;4(7):3979–3986. doi:10.1021/nn1008897
30. Haimes J, Kelley M Demonstration of a ΔΔCq calculation method to compute relative gene expression from qPCR data. GE Healthc; 2010. Available from: http://dharmacon.gelifesciences.com/uploaded files/resources/delta-cq-solaris-technote.pdf.
31. Ramakrishnan Minitha C, Suresh R, Kumar Maity U, et al. Magnetite nanoparticle decorated reduced graphene oxide composite as an efficient and recoverable adsorbent for the removal of cesium and strontium ions. *Ind Eng Chem Res*. 2018;57:58. doi:10.1021/acs.iecr.7b05340
32. Liu Y, Chen Z, Zhang Y, et al. Broadband and lightweight microwave absorber constructed by in situ growth of hierarchical CoFe 2 O 4/ reduced graphene oxide porous nanocomposites. *ACS Appl Mater Interfaces*. 2018;10(16):13860–13868. doi:10.1021/acsami.8b02137
33. Gurbani N, Han C-P, Marumoto K, et al. Biogenic reduction of graphene oxide: an efficient superparamagnetic material for photocatalytic hydrogen production. *ACS Appl Energy Mater*. 2018;1 (11):5907–5918. doi:10.1021/acsaem.8b00552
34. Jabbar A, Yasin G, Khan WQ, et al. Electrochemical deposition of nickel graphene composite coatings effect of deposition temperature on its surface morphology and corrosion resistance. *RSC Adv*. 2017;7 (49):31100–31109. doi:10.1039/c6ra28755g
35. Ferrari AC, Meyer JC, Scardaci V, et al. Raman spectrum of graphene and graphene layers. *Phys Rev Lett*. 2006;97(18). doi:10.1103/PhysRevLett.97.187401.
36. Wall M. The Raman spectroscopy of graphene and the determination of layer thickness. *Thermo Sci*. 2011;5.
37. Malard LM, Pimenta MA, Dresselhaus G, Dresselhaus MS. Raman spectroscopy in graphene. *Phys Rep*. 2009;473(5–6):51–87. doi:10.1016/j.physrep.2009.02.003
38. Zong M, Huang Y, Zhang N. Reduced graphene oxide-CoFe2O4 composite: synthesis and electromagnetic absorption properties. *Appl Surf Sci*. 2015;345:272–278. doi:10.1016/j.apsusc.2015.03.203
39. Liu Y, Guo H, Sun K, Jiang J. Magnetic CoOx@C-reduced graphene oxide composite with catalytic activity towards hydrogen generation. *Int J Hydrogen Energy*. 2019;44(52):28163–28172. doi:10.1016/j.ijhydene.2019.09.034
40. Wahajuddin AS. Superparamagnetic iron oxide nanoparticles: magnetic nanoplatforms as drug carriers. *Int J Nanomedicine*. 2012;7:3445–3471. doi:10.2147/IJN.S30320
41. Szymczyk A, Paszkiewicz S, Typek J, et al. Magnetic properties of poly(trimethylene terephthalate-block-poly(tetramethylene oxide) copolymer nanocomposites reinforced by graphene oxide–Fe3O4 hybrid nanoparticles. *Phys Status Solidi*. 2019;216(23):1900402. doi:10.1002/pssa.201900402
42. Vinodhkumar G, Wilson J, Inbanathan SSR, Potheher IV, Ashokkumar M, Peter AC. Solvothermal synthesis of magnetically separable reduced graphene oxide/Fe3O4 hybrid nanocomposites with enhanced photocatalytic properties. *Phys Rev B Condens Matter*. 2020;580:411752. doi:10.1016/j.physb.2019.411752
43. Hakimi M, Alimard P, Yousefi M. Green synthesis of reduced graphene oxide/Sr2CuMgFe 28O46 nanocomposite with tunable magnetic properties. *Ceram Int*. 2014;40(8PART A):11957–11961. doi:10.1016/j.ceramint.2014.04.032
44. Guo X, Mei N. Assessment of the toxic potential of graphene family nanomaterials. *J Food Drug Anal*. 2014;22(1):105–115. doi:10.1016/j.jfda.2014.01.009
45. Liao KH, Lin YS, MacOsko CW, Haynes CL. Cytotoxicity of graphene oxide and graphene in human erythrocytes and skin fibroblasts. *ACS Appl Mater Interfaces*. 2011;3(7):2607–2615. doi:10.1021/am200428v
46. Jiao G, He X, Li X, et al. Limitations of MTT and CCK-8 assay for evaluation of graphene cytotoxicity. *RSC Adv*. 2015;5(66):53240–53244. doi:10.1039/C5RA08958A
47. Li R, Guiney LM, Chang CH, et al. Surface oxidation of graphene oxide determines membrane damage, lipid peroxidation, and cytotoxicity in macrophages in a pulmonary toxicity model. *ACS Nano*. 2018;12(2):1390–1402. doi:10.1021/acsnano.7b07737
48. Das S, Singh S, Singh V, et al. Oxygenated functional group density on graphene oxide: its effect on cell toxicity. *Part Part Syst Char*. 2013;30(2):148–157. doi:10.1002/ppsc.201200066
49. Bonaccorso F, Sun Z, Hasan T, Ferrari AC. Graphene photonics and optoelectronics. *Nat Photonics*. 2010;4(9):611–622. doi:10.1038/nphoton.2010.186
50. Gurunathan S, Han JW, Eppakayala V, Kim JH. Biocompatibility of microbially reduced graphene oxide in primary mouse embryonic fibroblast cells. *Colloids Surf B Biointerfaces*. 2013;105:58–66. doi:10.1016/j.colsurfb.2012.12.036
51. Lingaraju K, Raja Naika H, Nagaraju G, Nagabhushana H. Biocompatible synthesis of reduced graphene oxide from Euphorbia heterophylla (L.) and their in-vitro cytotoxicity against human cancer cell lines. *Biotechnol Rep*. 2019;24:e00376. doi:10.1016/j.btre.2019.e00376
52. Luo L, Xu L, Zhao H. Biosynthesis of reduced graphene oxide and its in-vitro cytotoxicity against cervical cancer (HeLa) cell lines. *Mater Sci Eng C*. 2017;78:198–202. doi:10.1016/j.msec.2017.04.031
53. Li Y, Yuan H, von Dem Bussche A, et al. Graphene microsheets enter cells through spontaneous membrane penetration at edge asperities and corner sites. *Proc Natl Acad Sci U S A*. 2013;110 (30):12295–12300. doi:10.1073/pnas.1222276110
54. Duan G, Zhang Y, Luan B, et al. Graphene-induced pore formation on cell membranes. *Sci Rep*. 2017;7. doi:10.1038/srep42767
55. Badrigilan S, Shaabani B, Gharehaghaji N, Mesbahi A. Iron oxide/bismuth oxide nanocomposites coated by graphene quantum dots: "three-in-one" theranostic agents for simultaneous CT/MR imaging-guided in vitro photothermal therapy. *Photodiagnosis Photodyn Ther*. 2018;25:504–514. doi:10.1016/j.pdpdt.2018.10.021
56. Xie M, Zhang F, Peng H, et al. Layer-by-layer modification of magnetic graphene oxide by chitosan and sodium alginate with enhanced dispersibility for targeted drug delivery and photothermal therapy. *Colloids Surf B Biointerfaces*. 2019;176:462–470. doi:10.1016/j.colsurfb.2019.01.028
57. Geng B, Yang D, Pan D, et al. NIR-responsive carbon dots for efficient photothermal cancer therapy at low power densities. *Carbon*. 2018;134:153–162. doi:10.1016/j.carbon.2018.03.084
58. Zhang F, Xie M, Zhao Y, et al. Chitosan and dextran stabilized GO-iron oxide nanosheets with high dispersibility for chemotherapy and photothermal ablation. *Ceram Int*. 2019;45(5):5996–6003. doi:10.1016/j.ceramint.2018.12.070
59. Chang X, Zhang Y, Xu P, Zhang M, Wu H, Yang S. Graphene oxide/MnWO 4 nanocomposite for magnetic resonance/photoacoustic dual-model imaging and tumor photothermo-chemotherapy. *Carbon*. 2018;138:397–409. doi:10.1016/j.carbon.2018.07.058
60. Zhen SJ, Wang TT, Liu YX, Wu ZL, Zou HY, Huang CZ. Reduced graphene oxide coated Cu2−xSe nanoparticles for targeted chemo-photothermal therapy. *J Photochem Photobiol B Biol*. 2018;180:9–16. doi:10.1016/j.jphotobiol.2018.01.020
61. Su Y, Wang N, Liu B, et al. A phototheranostic nanoparticle for cancer therapy fabricated by BODIPY and graphene to realize photo-chemo synergistic therapy and fluorescence/photothermal imaging. *Dyes Pigm*. 2020;177:108262. doi:10.1016/j.dyepig.2020.108262
62. Liu J, Yuan X, Deng L, et al. Graphene oxide activated by 980 nm laser for cascading two-photon photodynamic therapy and photothermal therapy against breast cancer. *Appl Mater Today*. 2020;20:100665. doi:10.1016/j.apmt.2020.100665
63. Liu H, Li C, Qian Y, et al. Magnetic-induced graphene quantum dots for imaging-guided photothermal therapy in the second near-infrared window. *Biomaterials*. 2020;232:119700. doi:10.1016/j.biomaterials.2019.119700

64. Chang X, Zhang M, Wang C, Zhang J, Wu H, Yang S. Graphene oxide/BaHoF5/PEG nanocomposite for dual-modal imaging and heat shock protein inhibitor-sensitized tumor photothermal therapy. *Carbon*. 2020;158:372–385. doi:10.1016/j.carbon.2019.10.105
65. Marangon I, Ménard-Moyon C, Silva AKA, Bianco A, Luciani N, Gazeau F. Synergic mechanisms of photothermal and photodynamic therapies mediated by photosensitizer/carbon nanotube complexes. *Carbon*. 2016;97:110–123. doi:10.1016/j.carbon.2015.08.023
66. Salaheldin TA, Loutfy SA, Ramadan MA, Youssef T, Mousa SA. Ir-enhanced photothermal therapeutic effect of graphene magnetite nanocomposite on human liver cancer HepG2 cell model. *Int J Nanomedicine*. 2019;14:4397–4412. doi:10.2147/IJN.S196256
67. Schmitt E, Gehrmann M, Brunet M, Multhoff G, Garrido C. Intracellular and extracellular functions of heat shock proteins: repercussions in cancer therapy. *J Leukoc Biol*. 2007;81(1):15–27. doi:10.1189/jlb.0306167
68. Rizwan Younis M, Bing An R, Yin Y-C, Wang S, Ye D, Xia X-H. Plasmonic nanohybrid with high photothermal conversion efficiency for simultaneously effective antibacterial/anticancer photothermal therapy. *ACS Appl Bio Mater*. 2019;2(9):3942–3953. doi:10.1021/acsabm.9b00521
69. Tang X, Tan L, Shi K, et al. Gold nanorods together with HSP inhibitor-VER-155008 micelles for colon cancer mild-temperature photothermal therapy. *Acta Pharm Sin B*. 2018;8(4):587–601. doi:10.1016/j.apsb.2018.05.011
70. Gurunathan S, Kang M-H, Jeyaraj M, Kim J-H. Differential immunomodulatory effect of graphene oxide and vanillin-functionalized graphene oxide nanoparticles in human acute monocytic leukemia cell line (THP-1). *Int J Mol Sci*. 2019;20(2):247. doi:10.3390/ijms20020247
71. Choi YJ, Gurunathan S, Kim JH. Graphene oxide-silver nanocomposite enhances cytotoxic and apoptotic potential of salinomycin in human ovarian cancer stem cells (OvCSCs): a novel approach for cancer therapy. *Int J Mol Sci*. 2018;19(710):710. doi:10.3390/ijms19030710
72. Adams JM, Cory S. The Bcl-2-regulated apoptosis switch: mechanism and therapeutic potential. *Curr Opin Immunol*. 2009;19(5):488–496. doi:10.1016/j.coi.2007.05.004.The
73. Thapa RK, Byeon JH, Choi HG, Yong CS, Kim JO. PEGylated lipid bilayer-wrapped nano-graphene oxides for synergistic co-delivery of doxorubicin and rapamycin to prevent drug resistance in cancers. *Nanotechnology*. 2017;28(29):295101. doi:10.1088/1361-6528/aa7997
74. Placzek WJ, Wei J, Kitada S, Zhai D, Reed JC, Pellecchia M. A survey of the anti-apoptotic Bcl-2 subfamily expression in cancer types provides a platform to predict the efficacy of Bcl-2 antagonists in cancer therapy. *Cell Death Dis*. 2010;1(5):e40. doi:10.1038/cddis.2010.18